Practical Radiation Oncology (2015) 5, e9-e16

practical radiation oncology
pro
www.practicalradonc.org

Original Report

Long-term survival after treatment of glioblastoma multiforme with hyperfractionated concomitant boost proton beam therapy

Masashi Mizumoto PhD [a], Tetsuya Yamamoto PhD [b], Shingo Takano PhD [b], Eiichi Ishikawa PhD [b], Akira Matsumura PhD [b], Hitoshi Ishikawa PhD [a], Toshiyuki Okumura PhD [a], Hideyuki Sakurai PhD [a], Shin-Ichi Miyatake PhD [c], Koji Tsuboi PhD [a, b,*]

[a]*Proton Medical Research Center, University of Tsukuba, Tsukuba, Ibaraki, Japan*
[b]*Department of Neurosurgery, University of Tsukuba, Tsukuba, Ibaraki, Japan*
[c]*Department of Neurosurgery, Osaka Medical Collage, Osaka, Japan*

Received 1 December 2013; revised 24 March 2014; accepted 25 March 2014

Abstract

Purpose: Although conventional x-ray therapy of 60 Gy in 30 fractions is generally used in our institute as well as others, the prognosis of patients with glioblastoma multiforme (GBM) is poor. The purpose of this study was to evaluate the characteristics of long-term GBM survivors after postoperative hyperfractionated concomitant boost x-ray radiation therapy and proton beam therapy.

Methods and materials: Twenty-three of 81 GBM patients who met the eligible criteria and consented to the protocol were treated with x-ray radiation therapy (50.4 Gy in 28 fractions in T2-high areas) and proton beam therapy (46.2 GyE in 28 fractions in gadolinium-enhanced volumes >6 hours after x-ray radiation therapy) concurrent with nimustine hydrochloride or temozolomide.

Results: Treatment was completed in all patients within 38-50 days (median, 43 days). Six currently living patients (median follow-up period, 70.9 months) developed radiation necrosis without tumor recurrence. Of these, 5 underwent necrotomy and 2 received bevacizumab after necrotomy. Compared with the pretreatment status, the Karnofsky performance scale (KPS) for the 6 survivors decreased by 10%-30% at the last follow-up. However, radiation necrosis had been well controlled and 5 of 6 patients maintained a stable KPS without hospital care.

Conclusions: The results suggest that high-dose proton beam therapy could control GBM pathogenesis if the treatment area completely covers tumor infiltration. Although radiation necrosis was inevitable, the remaining brain volume was fairly well preserved in the long-term survivors.

Sources of support: This work was supported in part by Grants-in-Aid for Scientific Research (B) (24390286), Challenging Exploratory Research (24659556), Young Scientists (B) (25861064), and Scientific Research (C) (24591832) from the Ministry of Education, Science, Sports and Culture of Japan.
Conflicts of interest: None.
* Corresponding author. Proton Medical Research Center, Faculty of Medicine, University of Tsukuba, 1-1-1 Tennoudai, Tsukuba, Ibaraki, 305-8575 Japan.
E-mail address: tsuboi@pmrc.tsukuba.ac.jp (K. Tsuboi).

http://dx.doi.org/10.1016/j.prro.2014.03.012
1879-8500/

Introduction

The current standard of care for patients with glioblastoma multiforme (GBM) consists of maximum resection followed by 60 Gy of conventional x-ray radiation therapy concurrent with temozolomide administration.[1,2] Although a median survival period of 14.6 months has been achieved with this combination therapy, long-term survival rates are unsatisfactory, with a 2-year survival rate of only 26.5%.[2] Molecular targeted therapy[3,4] or immunotherapy in conjunction with conventional radiation therapy[5] with or without temozolomide was recently tested and found to have certain benefits in improving survival outcomes. Although these approaches are promising, their genuine clinical advantages require further investigation.

In radiation therapy, 60 Gy of x-rays in 30 fractions has been considered the maximum dose to avoid damage to normal brain tissue.[6] However, technologic advances in radiation therapy, such as proton beam therapy (PBT), intensity modulated radiation therapy, and stereotactic radiation therapy, have made it possible to deliver higher doses to the tumor while sparing healthy brain tissue.[7,8] This has led to the question of whether higher doses of radiation to the tumor can improve survival while maintaining quality of life for GBM patients. Several reports have suggested that high-dose radiation therapy can improve local control and survival in GBM patients.[7,8] Rusthoven et al[9] recently found that GBM patients with radiation necrosis at reoperation had improved survival compared with those without.

We previously reported that postoperative hyperfractionated concomitant boost PBT of 96.6 GyE in 56 fractions with nimustine hydrochloride was feasible and improved survival in GBM patients (median survival, 21.6 months).[10] We observed cases of long-term survivors without tumor recurrence during the follow-up of patients in this series and additional cases, and collected their serial magnetic resonance images over their entire clinical course. Thus, in this study we examined the characteristics of these long-term GBM survivors who underwent postoperative hyperfractionated concomitant boost PBT (96.6 GyE in 56 fractions).

Methods and materials

Patients

Between September 2001 and April 2009, 81 patients who were histologically diagnosed as GBM received postoperative radiation therapy at our institute. As our conventional standard radiation therapy we deliver 40 to 50 Gy in 20 to 25 fractions first to the area encompassing high intensity in T2-weighted MRI with a 2.0 cm margin. Subsequently, we add the remaining 10 to 20 Gy as a boost to the area encompassing contrast enhancement or the tumor bed plus a 2.0 cm margin, making a total dose of 60 Gy in 30 fractions. In some patients with poor general conditions such as Karnofsky performance scale (KPS) <40% or old age, consecutive daily treatment of 30 fractions is often difficult. In such cases, we reduce the total dose with smaller fraction numbers to shorten the treatment period. We usually deliver 45 Gy in 15 fractions to the contrast-enhanced area plus a 2 cm margin. Of these 81 patients, 58 received the aforementioned conventional radiation therapy; 41 were treated with doses from 60 to 61.2 Gy in 30 to 34 fractions, and 17 patients were treated with lower doses with smaller fraction numbers. The remaining 23 patients who met the eligible criteria[10,11] and consented on the basis of free will were prospectively enrolled in a phase 1/2 protocol for treatment with hyperfractionated concomitant boost PBT. A written informed consent based on each patient's will was obtained from all 23 patients (13 men, 10 women) prior to study enrollment. The patients had a median age of 56 years (range, 31-76 years). The KPS before PBT was 60% (n = 1), 70% (n = 5), 80% (n = 8), 90% (n = 7), and 100% (n = 2). Eight patients underwent partial resection and 15 underwent subtotal resection. The median MIB-1 labeling index was 29.6% (range, 3.8%-55.0%). The characteristics of the 23 patients are shown in Table 1.

Treatment methods

Treatment planning for PBT was performed using computed tomography images at 3-mm intervals in the treatment position. Proton beams were spread out and shaped with a ridge filter, double-scattering, multileaf collimators, and a custom-made bolus covering the target volume. All patients received hyperfractionated concomitant boost PBT after surgery.[10] The proton beam was generally delivered

Table 1 Characteristics of 23 patients

Characteristic	No.
Age (y)	31-76 (range)
	56 (median)
Sex	
Male	13
Female	10
Karnofsky performance status	
60	1
70	5
80	8
90	7
100	2
Extent of surgery	
Partial resection	8
Subtotal resection	15
MIB-1 labeling index (%)	3.8-55.0 (range)
	26.2 (median)

from 2 directions and all fields were treated daily. Clinical target volume 1 (CTV1) was defined as the area of contrast enhancement on magnetic resonance imaging (MRI) or the tumor bed, CTV2 was defined as CTV1 in addition to a 10-mm margin, and CTV3 was defined as the area surrounding edema determined by T2-weighted MRI or fluid-attenuated inversion recovery imaging. In the protocol, conventional x-ray radiation therapy or 250 MeV PBT (50.4 GyE in 28 fractions) was delivered to CTV3 in the morning. Concomitant boost PBT (23.1 GyE in 14 fractions) was delivered to CTV2 >6 hours after conventional radiation therapy, and subsequent PBT (23.1 GyE in 14 fractions) was delivered to CTV1. The planned target volume (PTV) was defined as CTV in addition to 5 mm for setup error. Total doses were 96.6 GyE in 56 fractions for PTV1, 73.5 GyE in 42 fractions for PTV2, and 50.4 Gy in 28 fractions for PTV3. The maximum dose was defined as 50 GyE to the optic chiasm and 60 GyE to the brain stem (dose to the entire brain stem was limited to 50 GyE).

Nimustine hydrochloride was administered intravenously at 80 mg/m^2 for 1 day in the first and fourth weeks of radiation therapy. Because concomitant chemotherapy was changed to temozolomide in August 2008, 2 patients were treated with hyperfractionated concomitant boost PBT concurrent with daily temozolomide (75 mg/m^2). Figure 1 shows a schematic diagram of our GBM treatment protocol.

Follow-up procedures and evaluation criteria

During treatment, acute treatment-related toxicities were assessed weekly in all patients. After completion of PBT, patients were evaluated by physical examination, MRI, and blood tests every 3 months for the first 2 years and every 6 months thereafter. The following 2 endpoints were evaluated: (1) MRI changes defined as development or enlargement of enhanced lesions on MRI to determine progression; and (2) death from any cause to estimate overall survival. The KPS was monitored before and after treatment and at the most recent follow-up. The Kaplan-Meier method was used to calculate MRI change-free and overall survival rates. Differences between groups were evaluated by the log-rank test. Acute and late treatment-related toxicities were assessed using the National Cancer Institute Common Terminology Criteria for Adverse Events, version 3.0, and the Radiation Therapy Oncology Group and European Organisation for Research and Treatment of Cancer (RTOG/EORTC) late radiation morbidity scoring scheme.[12] An in-field MRI change was defined as an event observed within CTV1 to which 96.6 GyE was delivered, a border MRI change was defined as an event within CTV2 or CTV3 to which 50.4-73.5 GyE was delivered, and an extra-field MRI change was defined as an event in the region outside CTV3.

Results

Background

All patients received x-ray radiation therapy and PBT within 3 months postoperatively. The period between surgery and initiation of radiation therapy was 15-87 days (median, 27 days), and x-ray radiation therapy and PBT

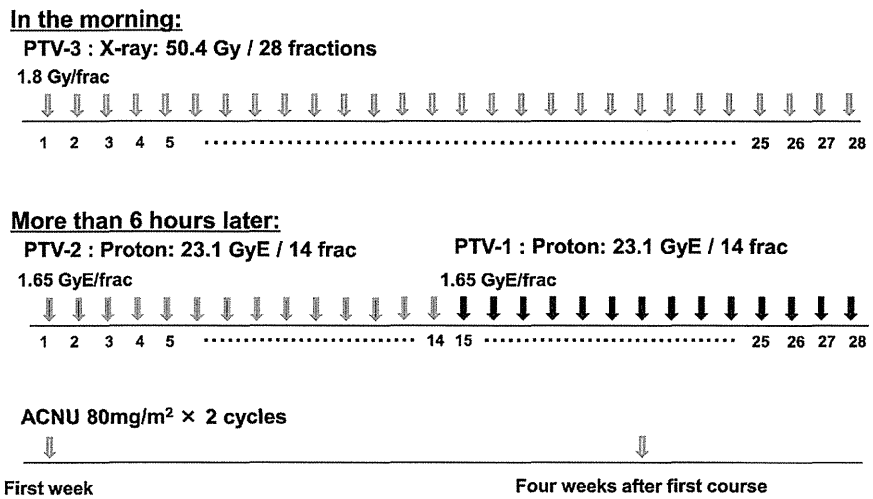

Figure 1 A schematic diagram of the treatment protocol for glioblastoma multiforme. Before August 2008, nimustine hydrochloride (ACNU) was administered intravenously at a dose of 80 mg/m^2 in the first and fourth weeks, thereafter, it was changed to concomitant daily use of temozolomide (75 mg/m^2). (PTV, planning target volume).

were administered over 38-50 days (median, 43 days). Of the 21 patients treated with nimustine hydrochloride, 17 received 2 cycles and 4 received 1 cycle. Of the 2 patients treated with temozolomide, 1 completed daily temozolomide concurrent with PBT and the other patient discontinued for 2 weeks because of neutropenia.

Toxicity

Grade 3 or higher acute hematologic toxicities occurred in 11 patients, probably due to nimustine hydrochloride.[10] Five patients with acute toxicity including nausea or headache were treated with corticosteroids during PBT. Grade 1 radiation dermatitis was observed in 2 patients and grade 2 was observed in 21 patients. In addition, all patients showed alopecia in the irradiated area. Late toxicity is discussed below.

Survival

The overall 1- and 2-year survival rates were 78% (95% CI, 61%-95%) and 43% (95% CI, 23%-63%), respectively, with a median survival period of 21.0 months (range, 5.5-81.0 months; 95% CI, 16.1-25.9 months; Fig 2). At the time of analysis, 6 patients were still alive with a median follow-up period of 70.9 months; all had survived >4 years after treatment. Fifteen patients died of tumor recurrence, and 2 died of unrelated diseases.

Magnetic resonance imaging changes

The 1- and 2-year MRI change-free survival rates of all 23 patients were 36% (95% CI, 16%-57%) and 13% (95% CI, 0%-28%), respectively (Fig 2). The median MRI change-free survival period was 9.0 months (range, 3.4-35.8 months; 95% CI, 7.0-10.9 months). the MRI changes defined as development or enlargement of enhanced lesion occurred in 20 patients, including 8 within CTV1 (96.6 GyE irradiation), 8 within CTV2 or CTV3 (≥50.4 GyE irradiation, but <96.6 GyE), and 4 outside the irradiated field. Six of the 8 patients with MRI changes within CTV1 had radiation necrosis without evidence of tumor recurrence. Five of these 6 patients were diagnosed by pathologic examination, and 1 patient was diagnosed by nuclear medicine study and MRI. All patients with MRI changes outside CTV1 were cases with tumor recurrence.

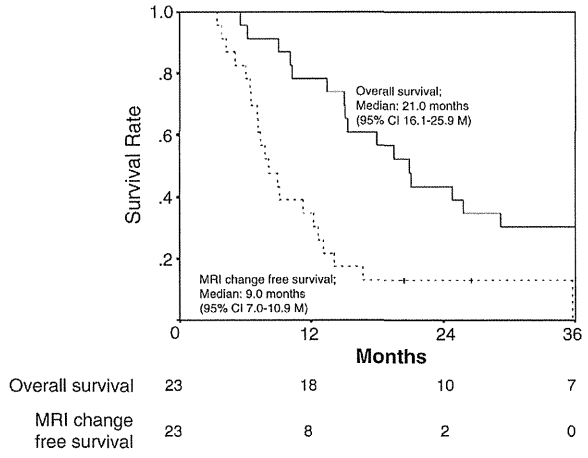

Figure 2 Kaplan-Meier estimates of overall survival and magnetic resonance imaging (MRI) change-free survival for all 23 patients. Tick marks indicate censored patients.

Long-term survivors

Upon follow-up of all 23 patients, 6 patients had radiation necrosis and 2 were diagnosed with leukoencephalopathy. The 6 patients with radiation necrosis survived at least 4 years after PBT without evidence of tumor recurrence. The median MRI change-free survival in patients with radiation necrosis was 12.7 months (range, 6.1-34.5 months; 95% CI, 6.6-18.8 months), whereas that of patients with GBM recurrence was 7.1 months (range, 3.4-12.6 months; 95% CI, 5.4-8.8 months; Fig 3). Two patients died at 19.5 and 25.8 months after radiation therapy without tumor recurrence on MRI. In these cases, marked cortical atrophy with diffuse white matter change was found on T2-weighted MRI, strongly indicating occurrence of leukoencephalopathy.

In survivors with radiation necrosis, KPS decreased by 10%-30% in the last follow-up compared with pretreatment KPS; however, 5 of the 6 patients maintained a stable KPS of >60%. The characteristics of the 6 survivors are shown in Table 2. The CTV1 in radiation necrosis cases was 13.4-46.2 cc (median, 20.6 cc) compared with 22.8-387.0 cc (median, 93.5 cc) in recurrent cases.

Case presentation (2 cases with or without bevacizumab treatment)

The typical clinical course for a long-term survivor with radiation necrosis is illustrated in Fig 4. Case 1 was a 46-year-old female with right temporal GBM (Fig 4A), and her pretreatment KPS was 90%. Following subtotal tumor resection, she received hyperfractionated concomitant boost PBT of 96.6 GyE in 56 fractions according to the protocol (Fig 4B,C). However, MRI changes appeared at the tumor bed 12 months after PBT, expanding slowly (Fig 4D,E). As neurologic symptoms progressed, a second surgery was performed 21 months after PBT (Fig 4F). The pathologic diagnosis at this time was radiation necrosis. In addition, because MRI showed that radiation necrosis had relapsed 42 months after PBT (Fig 4G), 6 courses of bevacizumab (5 mg/kg every 2 weeks) were performed.

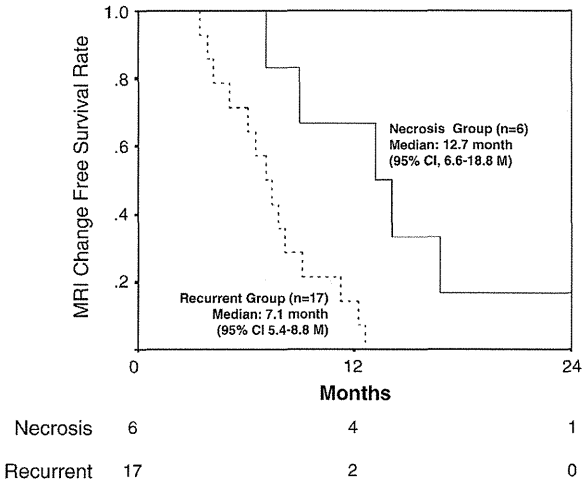

Figure 3 Kaplan-Meier estimates of magnetic resonance imaging (MRI) change-free survival for cases with radiation necrosis and recurrence. (CI, confidence interval.)

Following this therapy, radiation necrosis has been well controlled (Fig 4H) and her KPS maintained at 80%.

Case 2 was a 42-year-old woman with left temporal GBM (Fig 5A), and her pretreatment KPS was 100%. Following subtotal resection, she was treated with the same protocol as case 1 (Fig 5B,C). However, MRI changes appeared at the tumor bed 9 months after PBT (Fig 5D). Because tumor growth progressed gradually, the second surgery was performed 5 months later (Fig 5E), with a pathologic diagnosis of radiation necrosis. After the second resection, radiation necrosis remained stable for 40 months without further treatment (Fig 5F), and her KPS was maintained at 90%, manifesting slight sensory aphasia.

Discussion

Postoperative radiation therapy of 60 Gy in 30 fractions concurrent with temozolomide is the current standard of treatment for GBM patients. However, patient outcomes remain unsatisfactory.[1,2] Compared with conventional x-ray radiation therapy, the excellent dose concentricity of PBT allows delivery of higher doses to solid targets without residual damage to surrounding tissues,[13-19] possibly improving the prognosis of GBM patients. In a previous study,[10] we demonstrated that concomitant boost PBT of 96.6 GyE in 56 fractions improves patient survival with limited acute and late toxicity in GBM patients. Fitzeck et al[7] also found that a dose of 90 GyE with accelerated fractionation improved local GBM control and patient survival. In fact, exceptional control was achieved in the tissue area that received 90 GyE, whereas local recurrence was most frequently observed in areas that received $\leq$ 60-70 GyE. These results suggest that a PBT dose of $\geq$ 90 GyE may elicit effective control of GBM pathogenesis, in agreement with those of a study by McDonald et al,[11] which reported that >90% of failure patterns after conventional radiation therapy (60 Gy) plus temozolomide were central or in-field. Our study also demonstrated that 8 patients had MRI changes within the area irradiated with 96.6 GyE, and 6 of these patients were diagnosed with radiation necrosis without tumor recurrence. In contrast, the other 8 patients with MRI changes outside this area had only recurrence. Collectively, these results indicate that 96.6 GyE in 56 fractions can effectively control GBM growth, whereas $\leq$ 73.5 GyE is insufficient.

In our protocol, conventional x-ray radiation therapy or PBT (50.4 Gy in 28 fractions) was delivered to the T2-high area plus a 5-mm margin. Consequently, 4 patients showed recurrence at the marginal area in T2-weighted or fluid-attenuated inversion recovery MRI. This failure pattern may indicate an insufficient margination. Although we planned a 96.6 GyE distribution to the minimum essential area to avoid brain injury, a larger margination may be preferable, depending on tumor location and size, or additional diagnostic modalities, such as methionine positron emission computed tomography, should be applied to sufficiently cover the area of tumor invasion.

The median MRI change-free survival period (12.7 months) in the radiation necrosis group was approximately twice as long as that in the recurrent group. This indicates that radiation necrosis occurs later than tumor recurrence; thus, the incidence of radiation necrosis can be masked by tumor recurrence. Similarly, because conventional GBM treatment is associated with a low local control rate, the

Table 2 Clinical characteristics of 6 long-term survivors

No.	Age (y)	Sex	KPS before PBT (%)	CTV1 (cc)	Time to RN (mo)	Additional treatment for RN	Overall survival (mo)	Current KPS (%)
1	62	M	80	14.7	16.7	Surgery	76.8	60
2	49	F	90	46.2	7.1	Surgery	66.8	60
3	65	F	70	38.4	35.8	None	74.9	50
4	31	M	80	26.5	14.1	Surgery, bevacitumab	81.0	70
5	46	F	90	14.6	12.2	Surgery, bevacitumab	58.8	80
6	42	F	100	13.4	9.0	Surgery	52.8	90

CTV1, clinical target volume 1; KPS, Karnofsky performance status; PBT, proton beam therapy; RN, radiation necrosis.

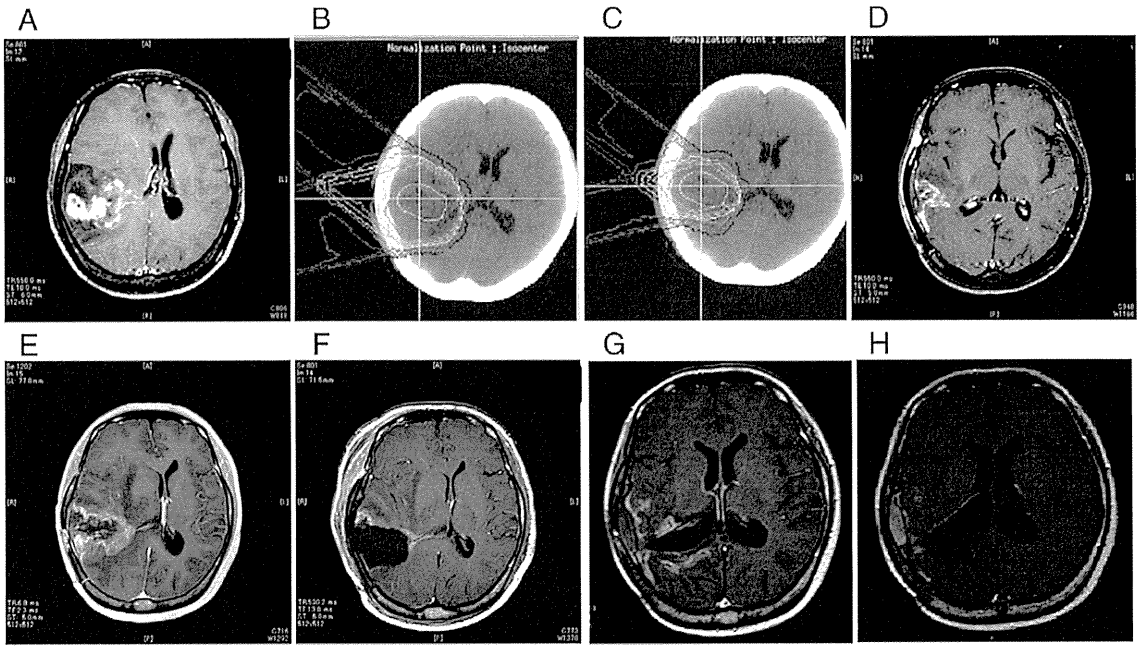

Figure 4 Case 1. Postcontrast T1-weighted magnetic resonance imaging (MRI) before the initial surgery (A). Isodose curves for proton beams representing 100%-10% of the prescribed dose at 10% intervals for the area of contrast enhancement on MRI plus a 10-mm margin (B) and for the area of contrast enhancement on MRI (C). Postcontrast T1-weighted MRI at 11 months after proton beam therapy (PBT) (D), at 20 months after PBT (E), after the second surgery (F), at 42 months after PBT (G), and at 51 months after PBT (H).

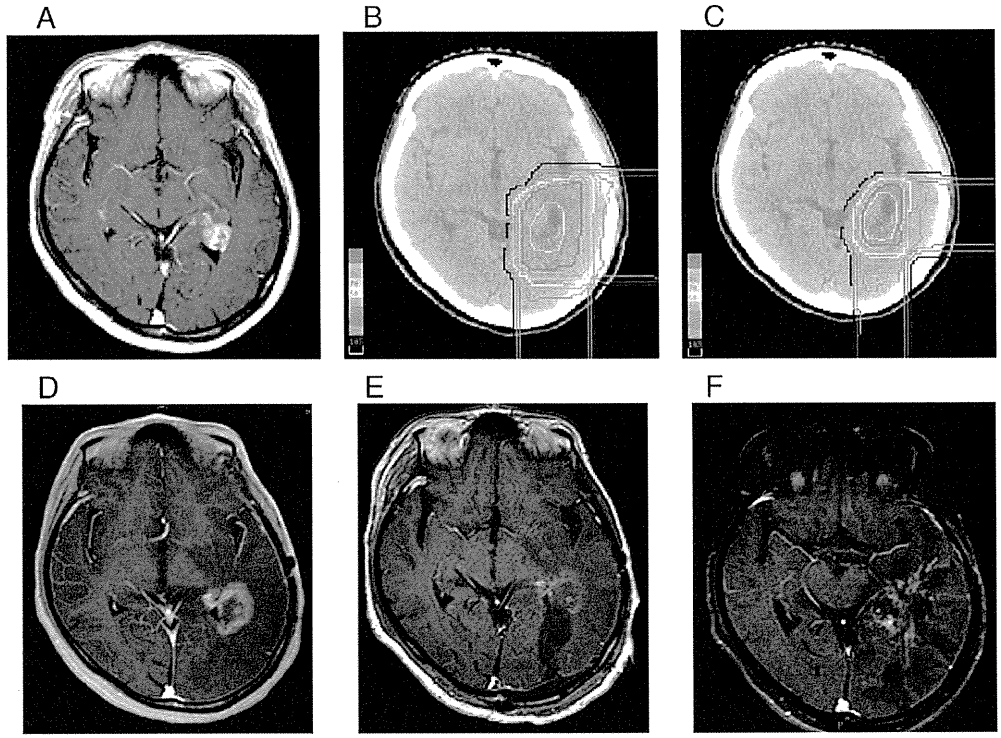

Figure 5 Case 2. Postcontrast T1-weighted magnetic resonance imaging (MRI) before the initial surgery (A). Isodose curves for proton beams representing 100%-10% of the prescribed dose at 10% intervals for the area of contrast enhancement on MRI plus a 10-mm margin (B) and for the area of contrast enhancement on MRI (C). Postcontrast T1-weighted MRI at 9 months after proton beam therapy (PBT) (D), after the second surgery (E), and at 40 months after PBT (F).

actual incidence of radiation necrosis in conventionally treated cases should be higher, although it has been reported that radiation necrosis of the brain occurs in approximately 5% of cases treated with 60 Gy x-ray radiation therapy.[20] Thus, radiation necrosis was observed in only 6 of our 23 patients (26%), maybe partly because of improved local control and subsequent prolonged survival with our treatment regimen.

Seizure or paralysis and coma are classified as grade 4 in the RTOG/EORTC late radiation morbidity scoring scheme.[12] Prevention of radiation necrosis is an important issue; however, occurrence of radiation necrosis may be inevitable using a 96.6 GyE protocol if long-term survival is achieved. We posit that the excellent dose concentricity of proton beams in our PBT method probably contributed to not only preservation of healthy brain tissue but also minimization of the volume of radiation necrosis. Moreover, we postulate that radiation necrosis could be more controllable and less fatal compared with GBM recurrence. In fact, our data showed that overall and MRI change-free survival in patients with radiation necrosis were significantly greater than those in patients with tumor recurrence. These findings are compatible with those of Rusthoven et al,[9] who found that patients with radiation necrosis at reoperation had improved survival compared with those with tumor recurrence in a study of grade 3-4 glioma treated with standard therapy.

Although necrotomy, hyperbaric oxygen therapy, anticoagulant therapy, and corticosteroid therapy have been used as treatments for radiation necrosis, a standard therapy has not yet been established.[21] At present, necrotomy is generally indicated for symptomatic radiation necrosis and 5 of the 6 patients who underwent necrotomy in our study had favorable outcomes. Recent reports suggest that bevacizumab, a monoclonal antibody to vascular endothelial growth factor, is effective for unresectable radiation necrosis.[22] On the basis of these reports, 2 patients in our series were treated with intravenous bevacizumab administration. Both patients showed good response in clinical symptoms and MRI, indicating that further prospective clinical trials are warranted for establishing bevacizumab as a treatment option for radiation necrosis.

Hypermethylation of the O6-methylguanine-DNA methyltransferase (MGMT) promoter is a favorable prognostic factor in GBM patients.[23] Minniti et al[24] found the rate of recurrence from the irradiated field was lower in cases with a methylated MGMT promoter region than in those with an unmethylated MGMT promoter region. Considering the present study did not examine the MGMT methylation status, further studies are needed to analyze the possible associations among MGMT promoter methylation, radiation necrosis, and long-term survival in GBM patients.

Our previously published retrospective data[25] showed that the median overall survival was 24.4 months (95% CI, 18.2-30.5 months) in 32 patients who received high-dose radiation therapy (the present treatment protocol or boron neutron capture therapy) compared with 14.2 months (95% CI, 10.0-18.3 months) in 35 patients treated with conventional radiation therapy (60.0-61.2 Gy in 30-34 fractions). Although KPS or tumor size in patients who received the above high-dose radiation therapy were favorable compared with the conventional cohort, we believe that dose escalation using modern treatment techniques is promising for improving GBM patient outcomes. Therefore, it is crucial to verify and optimize treatment indications using said high-dose radiation therapies.

In conclusion, our results indicate that high-dose 96.6 GyE concentric PBT has a high potential to improve survival in GBM patients if the treatment area completely covers the area of tumor infiltration. In addition, the remaining volume of healthy brain tissue was fairly well preserved in long-term survivors using our protocol. Although radiation necrosis is inevitable in the treated area, it may be controllable with necrotomy and bevacizumab administration.

References

1. Athanassiou H, Synodinou M, Maragoudakis E, et al. Randomized phase II study of temozolomide and radiotherapy compared with radiotherapy alone in newly diagnosed glioblastoma multiforme. *J Clin Oncol.* 2005;23:2372-2377.
2. Stupp R, Mason WP, van den Bent MJ, et al. Radiotherapy plus concomitant and adjuvant temozolomide for glioblastoma. *N Engl J Med.* 2005;352:987-996.
3. Moyal EC, Laprie A, Delannes M, et al. Phase I trial of tipifarnib (R115777) concurrent with radiotherapy in patients with glioblastoma multiforme. *Int J Radiat Oncol Biol Phys.* 2007;68:1396-1401.
4. Drappatz J, Norden AD, Wong ET, et al. Phase I study of vandetanib with radiotherapy and temozolomide for newly diagnosed glioblastoma. *Int J Radiat Oncol Biol Phys.* 2010;78:85-90.
5. Muragaki Y, Maruyama T, Iseki H, et al. Phase I/IIa trial of autologous formalin-fixed tumor vaccine concomitant with fractionated radiotherapy for newly diagnosed glioblastoma. *J Neurosurg.* 2011;115:248-255.
6. Fujii O, Soejima T, Kuwatsuka Y, et al. Supratentorial glioblastoma treated with radiotherapy: Use of the Radiation Therapy Oncology Group recursive partitioning analysis grouping for predicting survival. *Jpn J Clin Oncol.* 2010;40:726-731.
7. Fitzek MM, Thornton AF, Rabinov JD, et al. Accelerated fractionated proton/photon irradiation to 90 cobalt gray equivalent for glioblastoma multiforme: Results of a phase II prospective trial. *J Neurosurg.* 1999;91:251-260.
8. Tsien C, Moughan J, Michalski JM, et al. Phase I three-dimensional conformal radiation dose escalation study in newly diagnosed glioblastoma: Radiation Therapy Oncology Group Trial 98-03. *Int J Radiat Oncol Biol Phys.* 2009;73:699-708.
9. Rusthoven KE, Olsen C, Franklin W, et al. Favorable prognosis in patients with high-grade glioma with radiation necrosis: The University of Colorado reoperation series. *Int J Radiat Oncol Biol Phys.* 2011;81:211-217.
10. Mizumoto M, Tsuboi K, Igaki H, et al. Phase I/II trial of hyperfractionated concomitant boost proton beam therapy for supratentorial glioblastoma multiforme. *Int J Radiat Oncol Biol Phys.* 2010;77:98-105.

11. McDonald MW, Shu HK, Curran Jr WJ, Crocker IR. Pattern of failure after limited margin radiotherapy and temozolomide for glioblastoma. *Int J Radiat Oncol Biol Phys.* 2011;79:130-136.
12. Radiation Therapy Oncology Group. Available at: http://www.rtog.org/ResearchAssociates/AdverseEventReporting/RTOGEORTCLateRadiationMorbidityScoringSchema.aspx. Accessed July 20, 2013.
13. Knäusl B, Lütgendorf-Caucig C, Hopfgartner J, et al. Can treatment of pediatric Hodgkin's lymphoma be improved by PET imaging and proton therapy? *Strahlenther Onkol.* 2013;189:54-61.
14. Lorentini S, Amichetti M, Spiazzi L, et al. Adjuvant intensity-modulated proton therapy in malignant pleural mesothelioma. A comparison with intensity-modulated radiotherapy and a spot size variation assessment. *Strahlenther Onkol.* 2012;188:216-225.
15. Mizumoto M, Okumura T, Hashimoto T, et al. Proton beam therapy for hepatocellular carcinoma: A comparison of three treatment protocols. *Int J Radiat Oncol Biol Phys.* 2011;81:1039-1045.
16. Mizumoto M, Hashii H, Senarita M, et al. Proton beam therapy for malignancy in Bloom syndrome. *Strahlenther Onkol.* 2013;189:335-338.
17. Mizumoto M, Sugahara S, Nakayama H, et al. Clinical results of proton-beam therapy for locoregionally advanced esophageal cancer. *Strahlenther Onkol.* 2010;186:482-488.
18. Mizumoto M, Okumura T, Ishikawa E, et al. Reirradiation for recurrent malignant brain tumor with radiotherapy or proton beam therapy. *Strahlenther Onkol.* 2013;189:656-663.
19. Mizumoto M, Nakayama H, Tokita M, et al. Technical considerations for noncoplanar proton-beam therapy of patients with tumors proximal to the optic nerve. *Strahlenther Onkol.* 2010;186:36-39.
20. Ruben JD, Dally M, Bailey M, Smith R, McLean CA, Fedele P. Cerebral radiation necrosis: Incidence, outcomes, and risk factors with emphasis on radiation parameters and chemotherapy. *Int J Radiat Oncol Biol Phys.* 2006;65:499-508.
21. Bui QC, Lieber M, Withers HR, Corson K, van Rijnsoever M, Elsaleh H. The efficacy of hyperbaric oxygen therapy in the treatment of radiation-induced late side effects. *Int J Radiat Oncol Biol Phys.* 2004;60:871-878.
22. Levin VA, Bidaut L, Hou P, et al. Randomized double-blind placebo-controlled trial of bevacizumab therapy for radiation necrosis of the central nervous system. *Int J Radiat Oncol Biol Phys.* 2011;79:1487-1495.
23. Chandler KL, Prados MD, Malec M, Wilson CB. Long-term survival in patients with glioblastoma multiforme. *Neurosurgery.* 1993;32:716-720.
24. Minniti G, Amelio D, Amichetti M, et al. Patterns of failure and comparison of different target volume delineations in patients with glioblastoma treated with conformal radiotherapy plus concomitant and adjuvant temozolomide. *Radiother Oncol.* 2010;97:377-381.
25. Matsuda M, Yamamoto T, Ishikawa E, et al. Prognostic factors in glioblastoma multiforme patients receiving high-dose particle radiotherapy or conventional radiotherapy. *Br J Radiol.* 2011;84:54-60.

Brain Tumor Pathol
DOI 10.1007/s10014-014-0186-0

ORIGINAL ARTICLE

Development of a robust and sensitive pyrosequencing assay for the detection of *IDH1/2* mutations in gliomas

Hideyuki Arita · Yoshitaka Narita · Yuko Matsushita · Shintaro Fukushima · Akihiko Yoshida · Hirokazu Takami · Yasuji Miyakita · Makoto Ohno · Soichiro Shibui · Koichi Ichimura

Received: 17 February 2014 / Accepted: 30 March 2014

Abstract Assessment of the mutational status of the isocitrate dehydrogenase 1/2 (*IDH1/2*) gene has become an integral part of the standard diagnostic procedure and, therefore, needs to be accurate. This may, however, be compromised by various factors including the method of analysis and a low tumor cell content. We have developed a rapid, sensitive and robust assay to detect all types of mutation in either *IDH1* or *IDH2* using pyrosequencing. The efficacy of detecting mutation was evaluated using a panel of control plasmids representing all the different types of *IDH1/2* mutation and a set of 160 tumor specimens. The sensitivity of the assays was examined by a serial dilution analysis performed on samples containing various ratios of wild-type and mutant alleles. The pyrosequencing assay detected as little as 5 % of mutant alleles for most mutation types, while conventional Sanger sequencing required the presence of at least 20 % of mutant alleles for identifying mutations. The pyrosequencing assay detected *IDH1/2* mutations in three samples which were missed by Sanger sequencing due to their low tumor cell contents. Our assay is particularly useful for the analysis of a large number of specimens as in a retrospective clinical study for example.

Keywords Glioma · *IDH1* · *IDH2* · Pyrosequencing · Mutation detection

Electronic supplementary material The online version of this article (doi:10.1007/s10014-014-0186-0) contains supplementary material, which is available to authorized users.

H. Arita · Y. Narita · Y. Matsushita · Y. Miyakita · M. Ohno · S. Shibui
Department of Neurosurgery and Neuro-Oncology, National Cancer Center Hospital, Tokyo, Japan

H. Arita · S. Fukushima · H. Takami · K. Ichimura (✉)
Division of Brain Tumor Translational Research, National Cancer Center Research Institute, 5-1-1 Tsukiji, Chuo-ku, Tokyo 104-0045, Japan
e-mail: kichimur@ncc.go.jp

A. Yoshida
Department of Pathology and Clinical Laboratories, National Cancer Center Hospital, Tokyo, Japan

H. Takami
Department of Neurosurgery, University of Tokyo, 7-3-1 Hongo, Bunkyo-ku, Tokyo 113-0033, Japan

Introduction

Isocitrate dehydrogenase 1/2 (*IDH1/2*) mutations are regarded as one of the earliest genetic alterations in gliomagenesis, based on the mutation profiles of various subtypes of gliomas as well as primary and recurrent tumors [13, 30]. *IDH1/2* mutations are predominantly found in World Health Organization (WHO) grade II and III gliomas and secondary glioblastomas [3, 12, 30, 31]. Mutations in *IDH1/2* have been associated with longer survival in every histological type or every WHO grade [25, 31]. It is now clear that the *IDH1/2* mutational status defines two biologically and clinically distinct groups of gliomas. Determining the mutational status of *IDH1/2* has become a part of the standard diagnostic procedure and may be used for stratification in clinical trials as it is one of the major prognostic factors in gliomas [28]. It is, therefore, absolutely essential that the status of *IDH1/2* must be accurately and robustly assessed. Various factors may, however, potentially compromise the authenticity of the results; these include the method of analysis, the type of tumor specimen [frozen or formalin-fixed paraffin-embedded (FFPE) samples] and the tumor cell content.

Published online: 19 April 2014

Almost all reported mutations of *IDH1/2* in gliomas are heterozygous missense affecting either codon 132 in *IDH1* or codon 172 in *IDH2* [11]. About 90 % of all *IDH1/2* mutations are c.395G>A (R132H) in *IDH1* [11]. Other *IDH1* mutations include c.394C>T (R132C), c.394C>A (R132S), c.394C>G (R132G), c.395G>T (R132L), R132P (nucleotide change not reported in the original article) and R132V (c.394C>G and c.395G>T); the latter two mutations reported only in single cases [9, 29]. *IDH2* c.515G>A (R172K) accounts for about 3 % of all *IDH1/2* mutations, and other *IDH2* mutations include c.515G>T (R172M), c.514A>T (R172W), c.516G>C (R172S) and c.514A>G (R172G) [11].

Direct sequencing and immunohistochemistry (IHC) are the most widely used methods for assessing the *IDH1/2* status. Sanger sequencing, however, has the limitation of being unable to detect mutations in tumor samples that contain extensive necrosis or are contaminated with non-neoplastic cells; the accuracy of Sanger sequencing, therefore, largely depends on the quality of the sample [1, 5]. For IHC, two specific antibodies for the mutant R132H, DIA-H09 and IMab-1, are commercially available and well-characterized [4, 15]. The significant advantage that IHC has over Sanger sequencing is that FFPE samples are readily available through routine histopathological examination. IHC, however, can only detect the mutation specific to the antibody used. Antibodies specific for mutations other than R132H have also been developed [14, 16], however, their efficacy needs to be further validated in clinic.

We have developed rapid and robust assays for the detection of *IDH1/2* mutations using pyrosequencing, which is a sequence-by-synthesis technique based on the luciferase–luciferin light release as a signal for nucleotide incorporation into target DNA [24]. Our novel assays enable the detection of all reported mutations in *IDH1* or *IDH2* at a single run for each gene. We describe the details of our original assay and evaluate its potential efficacy in clinical application.

Materials and methods

DNA samples

Frozen tissue samples from a total of 160 glioma cases operated at the National Cancer Center Hospital (Tokyo, Japan) were included in this study; 29 diffuse astrocytomas, 11 oligoastrocytomas, 2 oligodendrogliomas, 28 anaplastic astrocytomas, 21 anaplastic oligoastrocytomas, 8 anaplastic oligodendrogliomas, 55 primary glioblastomas and 6 secondary glioblastomas. Matched FFPE samples were available for analysis in nineteen cases (Supplementary Table 1). Twenty blood samples were also analyzed as a normal control. The study was approved by the local institutional review board. Histological diagnoses were made according to the WHO classification [18]. A DNeasy Blood & Tissue Kit (Qiagen, Tokyo, Japan) was used to extract DNA.

Control plasmids

All control plasmids that contain every single type of mutation except *IDH1* R132L (see below) were generated by subcloning the mutated sequences from the tumor samples (obtained from the Department of Pathology, University of Cambridge [12]). Briefly, after amplifying the genomic DNA containing the different types of *IDH1/2* mutation, the polymerase chain reaction (PCR) product was subcloned into the pMD20-T vector by a TA cloning procedure using the 10X A-Attachment mix (TOYOBO, Osaka, Japan) and a Mighty Cloning Kit (TAKARA Bio Inc., Tokyo, Japan) according to the manufacturers' recommendations. The control plasmids for R132H, R132C, R132S and R132G in *IDH1*, and R172K, R172M, R172W and R172S in *IDH2* were all generated using the method described above. The plasmid containing the *IDH1* R132L (c.395G>T) mutation was generated by site-directed mutagenesis because no samples in our tumor cohort had this mutation. For this procedure, 50 ng of plasmids with wild-type *IDH1* were unidirectionally amplified using a complementary pair of oligonucleotides containing the mutation, and the non-mutant *dam*-methylated template plasmid DNA was digested using the DpnI restriction enzyme (New England Biolabs Japan Inc., Tokyo, Japan) before the newly synthesized mutated construct is transformed into *E. coli*.

Pyrosequencing

Polymerase chain reaction primers were designed for amplifying relatively small DNA fragments, either 86 bp for *IDH1* or 85 bp for *IDH2* sequences, containing the targeted region so that the assay could potentially be used for DNA extracted from archival tissues. Detailed information about the primers is given in Table 1. Templates for pyrosequencing were prepared by amplifying genomic DNA (10 ng) with primers that were biotinylated for the template strands. The 25 μl PCR mix included 62.5 μM of each dNTP, 0.625 units of Ampli Taq Gold 360 DNA polymerase and 0.5 μM of primers for *IDH1/2* each as per manufacturer's recommendations. The $MgCl_2$ concentration of the PCR mix was optimized for each primer set; 2 mM for *IDH1* and 1.5 mM for *IDH2*. The thermal cycling conditions for amplification were as follows: one cycle of initial denaturation at 95 °C for 10 min, followed

Table 1 Sequences of the primers for PCR for pyrosequencing, Sanger sequencing, and the pyrosequencing assays

Procedure	Sequence
PCR for pyrosequencing	
For *IDH1* (product length 86 bp)	
Forward primer (PC6041)	CAAAAATATCCCCCGGCTTG
Reverse primer (PC6042)	bio-CAACATGACTTACTTGATCCCC
For *IDH2* (product length 85 bp)	
Forward primer (PC6099)	ACATCCCACGCCTAGTCCC
Reverse primer (PC6100)	bio-TCTCCACCCTGGCCTACCTG
Pyrosequencing	
For *IDH1*	
Primer (P0125)	ACCTATCATCATAGGT
Sequence to analyze	CDTCATGCTTAT
Dispensation order	GATCATGTCATG
Assay type	AQ assay
For *IDH2*	
Primer (P0126)	CCCATCACCATTGGC
Sequence to analyze	ANGCAC
Dispensation order	TATGTCACGCAC
Assay type	AQ assay
Sanger sequencing [10]	
For *IDH1* (product length 254 bp)	
Forward primer (IDH1 fc)	ACCAAATGGCACCATACGA
Reverse primer (IDH1 rc)	TTCATACCTTGCTTAATGGGTGT
For *IDH2* (product length 293 bp)	
Forward primer (IDH2 fc)	GCTGCAGTGGGACCACTATT
Reverse primer (IDH2 rc)	TGTGGCCTTGTACTGCAGAG

by 35 cycles 95 °C 30 s, 55 °C 30 s, and 72 °C 30 s. An additional cycle at 72 °C for 5 min was added to complete the elongation step. Amplification of the PCR products was confirmed by running 3 μl of the reaction mix on an agarose gel.

Single-stranded templates for pyrosequencing were prepared as per manufacturer's recommendations using 20 μl of PCR template (Qiagen, Tokyo, Japan). The purified single-stranded PCR products were denatured and annealed to 15 pmol of pyrosequencing primer. Pyrosequencing was performed using the PyroGold Q96 SQA Reagents and the PyroMark Q96 software (version 2.5.7) on a PSQ96 pyrosequencer (Qiagen, Tokyo, Japan) according to the manufacturer's recommendations. The data were analyzed using the PyroMark Q96 software. The 3′ end of the pyrosequencing primers was designed immediately upstream of each hotspot. The dispensation orders for pyrosequencing were designed so that all possible mutations at the first two positions of codon 132 of *IDH1* and codon 172 of *IDH2* could be identified in a single assay for each gene (indicated in Table 1). An AQ analysis, which is an analysis mode within the PyroMark Q96 software, was performed so that the percentage of mutant allele could be quantified in this assay.

Sanger sequencing

Templates for Sanger sequencing were prepared by amplifying 10 ng of genomic DNA with a set of primers (Table 1). The 10 μl PCR mix included 2.0 mM of $MgCl_2$, 125 μM of each dNTP, 0.5 units of Ampli Taq Gold 360 DNA polymerase (Applied Biosystems, Foster City, CA, USA) and 0.5 μM of primer pairs (IDH1 fc and rc for *IDH1*, or IDH2 fc and rc for *IDH2* [10]). The same primer pair as the one used for *IDH1* pyrosequencing (PC6041 and PC6042) was used in a single FFPE sample (DA068) which was not sufficiently amplified by the standard primer pairs for Sanger. The thermal cycling for amplification was as follows: one cycle of initial denaturation at 95 °C for 10 min, followed by 40 cycles of 95 °C 30 s, 55 °C 30 s, 72 °C 30 s with an additional cycle of 72 °C for 7 min. Amplification of the 254 bp (*IDH1*) or 293 bp (*IDH2*) product was confirmed by running 3 μl of the reaction mix on an agarose gel. After purification using ExoSAP (Affymetrix Japan KK, Tokyo, Japan) as per manufacturer's recommendations, cycle sequencing was carried out using the BigDye Terminator v3.1 cycle sequencing kit (Applied Biosystems, Foster City, CA, USA) and the same forward primer (IDH1 fc, PC6041 or IDH2 fc) as the amplification of genomic DNA.

The thermal cycling for amplification was as follows: 25 cycles of 96 °C 10 s, 50 °C 15 s, and 60 °C 4 min.

Immunohistochemistry

Immunohistochemistry using a mouse monoclonal anti-human IDH1 R132H antibody (H09, Dianova, Hamburg, Germany) was performed by a polymeric method of EnVision FLEX system (Dako Japan Inc, Tokyo, Japan) with an automatic staining machine (Auto-stainer Link 48, Dako Japan Inc, Tokyo, Japan) as previously reported [8]. The presence of positive granular cytoplasmic staining in the tumor cells was judged as being indicative of mutant *IDH1*.

Results

The sensitivity and specificity of the newly developed pyrosequencing assays for *IDH1* and *IDH2* mutation

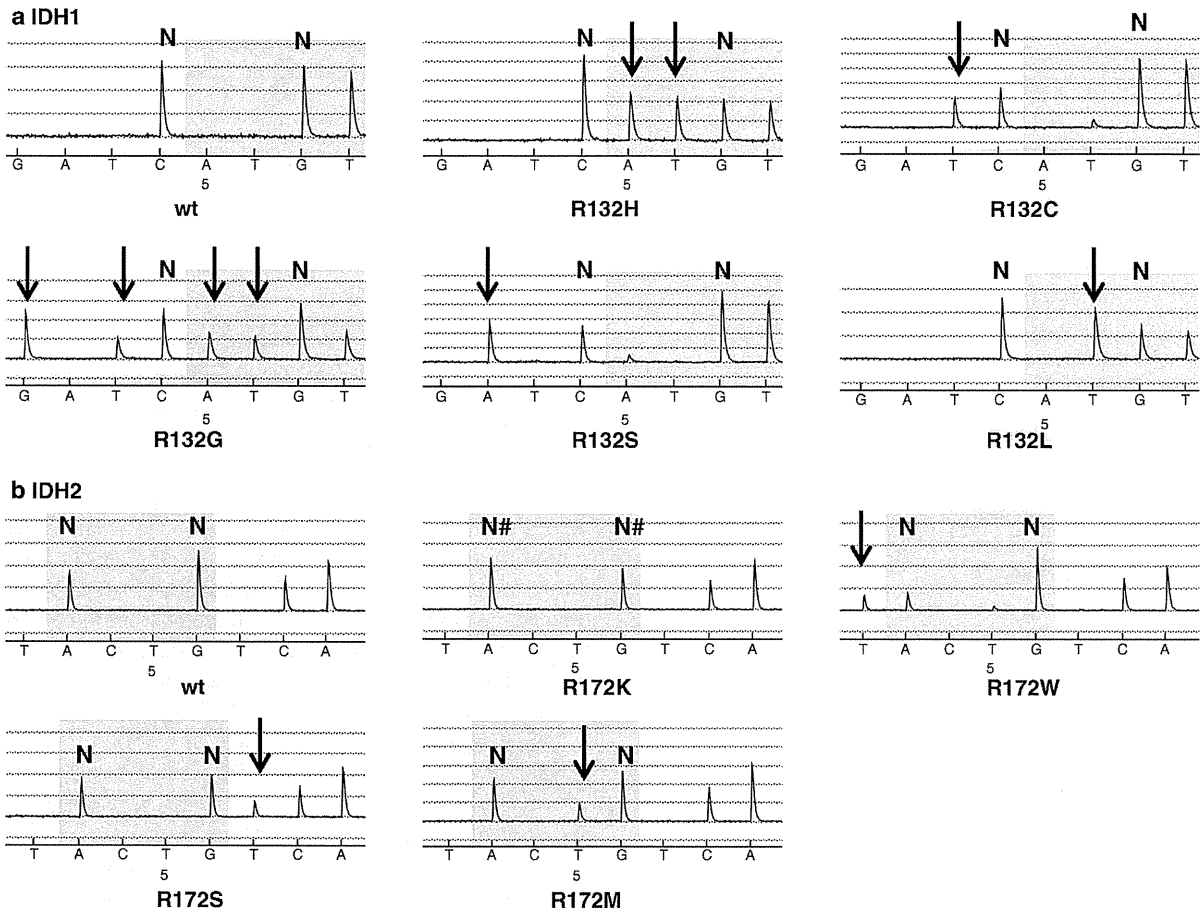

Fig. 1 Pyrograms for each *IDH1/2* mutation. Samples containing equal amounts of wild-type and mutant DNA were subjected to the pyrosequencing assays. The pyrograms show the mutation-specific pattern obtained for each mutation in *IDH1* (**a**) or *IDH2* (**b**) indicated by the *arrows*. "N" denotes the normal peaks. In this assay, all the mutations but *IDH2* R172K have their specific patterns of peaks which are not present in the wild-type samples. The *IDH2* R172K mutation is detected as a higher peak at the 3rd dispensation (*A*) and a lower peak at the 6th dispensation (*G*); those peaks are marked by "N#"

screening were first validated using the control DNA mixture that contains equal amounts of the wild-type and mutated plasmid constructs. All *IDH1* mutations were successfully identified by detecting mutant-specific peaks in a single assay. As shown in Fig. 1a, only one peak at the 4th dispensation (C) was observed among the first 5 dispensations in the pyrogram of the wild-type *IDH1*, while abnormal peaks were observed either at the 1st, 2nd, 3rd, 5th or 6th dispensation only in the mutated DNA, but not in the wild type. As for *IDH2*, two peaks at the 3rd (A) and 6th (G) dispensations were observed in the pyrogram of the wild type, while abnormal peaks unique to each mutation were observed at the 2nd, 5th and 7th dispensations in R172W, R172M and R172S mutants, respectively (Fig. 1b). The *IDH2* R172K mutation could be detected by a peak twice as high as the wild type at the 3rd dispensation and a peak half as high as the wild type at the 6th dispensation. Thus, our assays identify all mutants of *IDH1/2*, except the R172K mutant, by the presence of abnormal peaks which should be absent in the wild-type *IDH2*. The R172K mutation can also be detected by quantifying the mutant allele frequency using an AQ analysis as described below.

Twenty blood samples were then subjected to pyrosequencing to determine the threshold of normal variation. For the c.395 position of *IDH1*, the mean frequency of A, T, G (wild type) and C was 0 %, 0.078 ± 0.065 % (range 0–0.27 %), 99.9 ± 0.1 % (range 99.7–100 %) and 0 %, respectively. For the c.514 position of *IDH2*, the mean frequency of A, T, G (wild type) and C was 7.0 ± 2.6 % (range 3.6–13.9 %), 0 %, 93.0 ± 2.6 % (range 86.1–96.4 %) and 0 %, respectively. Based on the

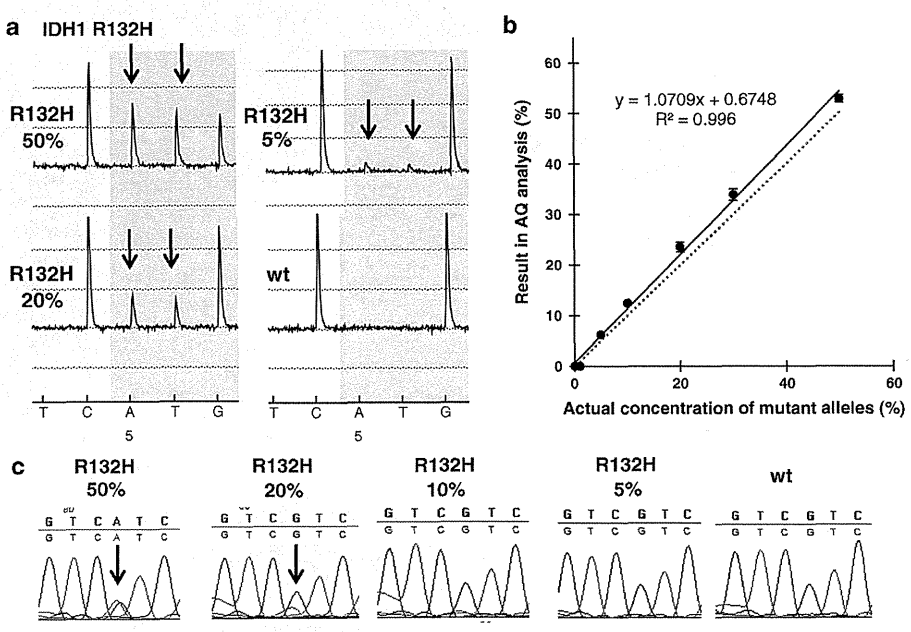

Fig. 2 Serial dilution analysis for the evaluation of the sensitivity in detecting R132H mutation in *IDH1*. **a** A mixture of the control plasmid constructs containing variable ratios of wild-type and R132H mutant alleles of *IDH1* was subjected to pyrosequencing. Even 5 % of mutant allele could be detected as a peak as shown in the pyrogram (the mutated peaks are indicated by *arrows*). **b** The triplicated results of the pyrosequencing assay plotted against the expected concentration showing a very high concordance ($R^2 = 0.996$). **c** The peak of the mutant allele in the Sanger sequencing chromatogram was obscure in samples containing 10 % or less mutant DNA

maximum error ratio in the normal blood controls, the mutant allele frequency of 0.27 % or less for *IDH1* and 13.9 % or less for *IDH2* will be considered as within normal variation.

Next, serial dilution experiments were performed to assess the sensitivity of the pyrosequencing assay to detect *IDH1/2* mutations. Pyrosequencing and Sanger sequencing were performed on either R132H of *IDH1* or R172K of *IDH2* mutant construct serially diluted with the wild-type plasmid to achieve ratios of mutant DNA of 0, 1, 5, 10, 20, 30 or 50 % in triplicate as follows. The presence of the *IDH1* R132H mutant allele was detected as a clearly distinct peak in the pyrogram in samples containing 5 % or more mutant DNA (Fig. 2a) whereas the mutant peak in the chromatograms obtained from direct sequencing was apparent only in samples with 20 % or more mutant DNA (Fig. 2c). The mean measured frequencies of the triplicate experiments showed a strong linear correlation, being almost equal to the actual frequencies of the mutant alleles ($R^2 = 0.996, p < 0.0001$) (Fig. 2b). Based on the threshold defined in the above experiments, the samples showing a mutant allele ratio of 5 % or more were judged to be mutated in this assay. This sensitivity was remarkably comparable with the value found in previously reported assays [7, 26]. As for R172K in *IDH2*, because it was not possible to design an assay to detect the mutation by the presence of a unique peak, this mutation could nevertheless be characterized by quantifying the peak common to wild-type and mutated alleles using the AQ analysis. The mean frequencies of triplicate experiments were slightly higher, nonetheless strongly correlated with the expected frequencies of the mutant alleles ([Percentage in AQ analysis] = 1.07 * [Actual percentage] +4.13, $R^2 = 0.998, p < 0.0001$) (Fig. 3b). Based on the results of the blood samples, the samples showing a mutant allele concentration of 10 % or above were considered as mutated in this assay. In Sanger sequencing, the mutant allele could only be detected in samples containing at least 10 % of the mutated DNA (Fig. 3c).

Finally, the pyrosequencing assay and Sanger sequencing were compared in a series of glioma samples to validate the efficacy of detecting mutations on genuine clinical cases. *IDH1* was Sanger sequenced in all 160 cases and *IDH2* in selected cases mainly consisted of those without *IDH1* mutations ($n = 113$). The result of each case is shown in Supplementary Table 1. The pyrosequencing-based analysis for *IDH1* detected mutations in 75 cases (74 cases with R132H and a single case with R132S), while the Sanger sequencing failed to detect three R132H mutant cases (DA068, AA067 and OA 040). The frequencies of mutant alleles measured by pyrosequencing were low in the three discordant cases (10.8–16.2 %), suggesting that those samples contained a low percentage of tumor cells. The results of the pyrosequencing and Sanger sequencing screening for *IDH2*, which identified R172K mutations in 4 tumors (Supplementary Table 1), were identical in all cases analyzed.

Immunohistochemistry was performed on 69 cases including the three discordant cases between Sanger sequencing and pyrosequencing. IHC and pyrosequencing results were concordant in all cases. To ensure that exactly the same specimen was used for comparison, the three

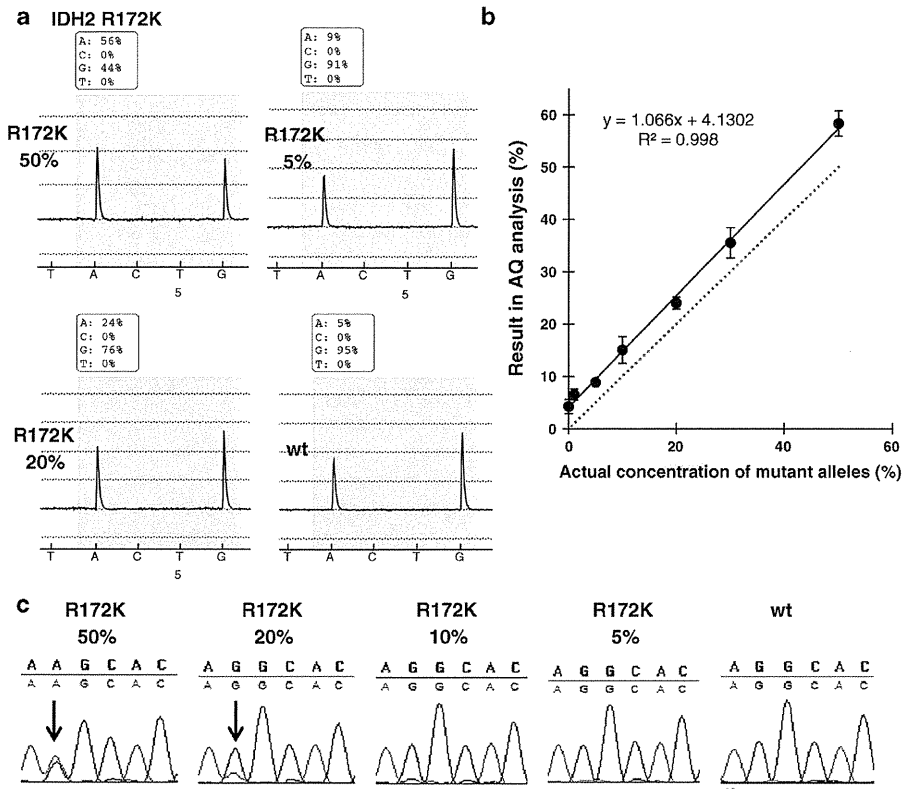

Fig. 3 Serial dilution analysis for the evaluation of the sensitivity in detecting R172K mutation in *IDH2*. **a** Samples containing variable concentrations of wild-type and R172K mutant alleles of *IDH2* were subjected to pyrosequencing. For detection of this mutation, the assessment was based on the allele ratio calculated by the AQ assay as shown in the *insets*. **b** The pyrosequencing assay gives slightly higher values, nonetheless it showed a high concordance with the expected concentration. **c** The peak of mutant allele in the Sanger sequencing (*arrows*) was obscure in samples containing 10 % or less mutant DNA

discordant cases between pyrosequencing and Sanger sequencing (DA068, AA067 and OA 040) were subjected to a new round of Sanger sequencing and pyrosequencing using DNA extracted from sequentially sectioned FFPE samples which were used for IHC. In one of the three previously discordant cases (DA068), the R132H mutation in *IDH1* was detected by pyrosequencing and IHC, but not by Sanger sequencing (Fig. 4). In the other two previously discordant cases (AA067 and OA040), the IHC was found positive and the repeated Sanger sequencing also confirmed the presence of the mutations as a minor allele.

To test whether pyrosequencing is applicable to FFPE, the DNAs extracted from a further 16 matched FFPE specimens were subjected to pyrosequencing for *IDH1*. The results from FFPE and frozen samples were consistent in all cases examined (Supplementary Table 1).

Discussion

The purpose of this paper is to present and discuss in detail a novel pyrosequencing assay for the mutational analysis of *IDH1/2*. This protocol was specifically designed with the clinical setting in mind and should, therefore, be quickly and easily implemented in any laboratories equipped with a pyrosequencer. The assay is fully compatible with Sanger sequencing and shown to be robust, efficient and more sensitive in detecting low-level mutations than the Sanger sequencing method. This assay is particularly useful for the genetic screening of *IDH1/2* mutations in a large tumor cohort as exemplified by its successful application in our recent study of gliomas [2].

Pyrosequencing has been applied to various genetic analyses including mutation detection at hotspots in *KRAS*, or quantitative measurement of methylation levels in the CpG island of the O^6-Methylguanine-DNA methyltransferase (*MGMT*) gene using bisulfite-modified DNA [19, 21, 23]. Several previous studies have also reported the use of pyrosequencing for the detection of *IDH1/2* mutations [6, 7, 17, 20, 26, 27, 32]. These studies mainly focused on the feasibility of detecting *IDH1/2* mutations by pyrosequencing or the clinical significance of these mutations, however, full details of the assay were not given, which prevented independent validation of the assay by others [6, 7, 20, 27, 32]. Our novel pyrosequencing assays for detecting *IDH1/2* mutations are fully validated using engineered controls for almost all known *IDH1* R132 and *IDH2* R172 mutations. We also strived to provide all the technical details to allow an immediate replication of the technique. The robustness of a pyrosequencing-based

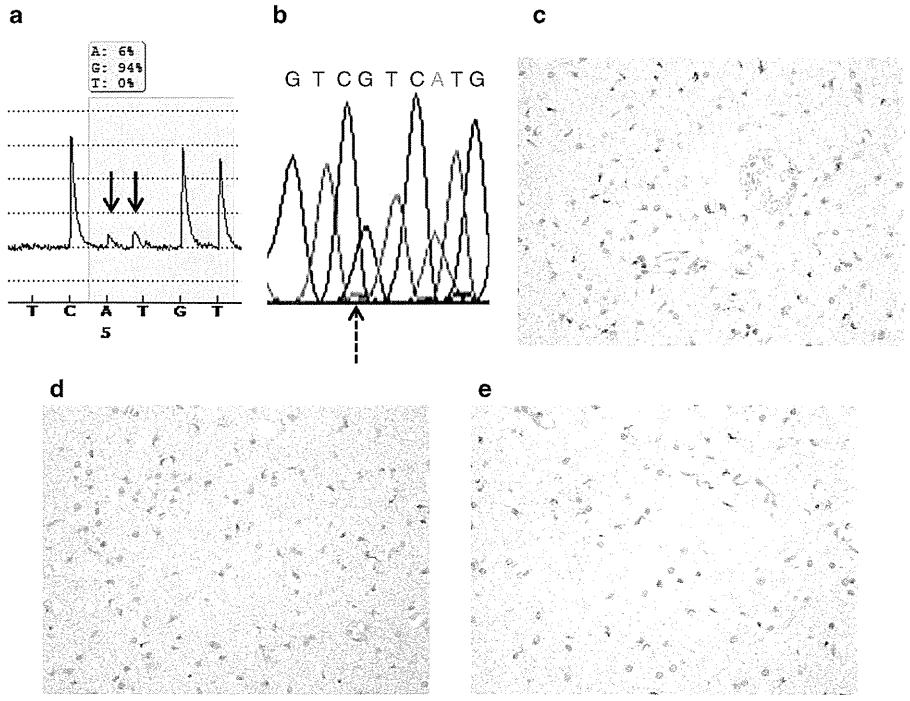

Fig. 4 The discordant case. A single case (DA068) showed discordance between pyrosequencing, Sanger sequencing and immunohistochemistry for *IDH1*. **a** The peaks indicating the R132H mutation (*arrows*) are shown in the pyrogram. The ratio of the mutant alleles was calculated to be 6.48 % by the AQ assay, suggesting the low density of tumor cells in this specimen. **b** A peak of adenine (*green*) at the hotspot (*broken arrow*) indicating the R132H mutation was obscure and hard to distinguish from non-specific peaks in the chromatogram. The cytoplasm of infiltrating tumor cells was positively stained in IHC using an antibody against the R132H mutation (original magnification ×400). The overall tumor cell content of this FFPE sample was low. Three separate areas with different tumor cell contents are shown (**c** the highest in this specimen, **d** intermediate, **e** low)

analysis depends on the design of the dispensation order, which determines the various types of mutation detectable by the assay. We successfully detected virtually all types of the known reported *IDH1/2* mutations using a single assay each for *IDH1* and *2*. Some of the previous studies applied more than one assay for this purpose [26]. Moreover, all mutations except one, *IDH2* R172K, are detected by the presence of mutation-specific peaks which are absent in the wild-type samples, making the assay highly sensitive. Not enough detailed information such as the dispensation order for example was provided in other previous studies [17]. With our novel assay, we set to achieve a fast and easy implementation aimed at the clinical setting.

We demonstrated the sensitivity and quantitativity of our assays by serial dilution analysis. It is a known fact that the sensitivity of conventional Sanger sequencing may be compromised by contamination of the samples with non-neoplastic tissues. Our results suggest that the conventional Sanger technique requires the presence of at least 20 % of the mutant alleles for the detection to be reliable [29]. By contrast, our assay detects as little as 5 % of the mutant alleles, and this sensitivity is comparable to previous studies [7, 26]. Glioma tissues often have a heterogeneous cell contents due to the invasive nature of the tumor into the surrounding brain tissue as well as its tendency to attract microglia infiltration [22]. The detection of *IDH1/2* mutations in samples containing a low percentage of tumor cells is challenging, but it is an absolute necessity for its clinical application. We showed that our pyrosequencing assays were applicable to FFPE samples, which are consistent with previous reports [6, 7, 26].

An optimal method for *IDH1/2* mutation testing remains under debate [28]. Some studies found that the results obtained by pyrosequencing were identical to those generated by Sanger sequencing [7, 26]. One study reported comparable frequencies of *IDH1/2* mutations detected between pyrosequencing, Sanger sequencing and IHC [17]. In the present study, the result of IHC was identical to that of pyrosequencing, while Sanger sequencing failed to detect mutations in three cases (4 % of *IDH1* mutated cases). The discordance between pyrosequencing and Sanger sequencing was attributable to the low tumor contents in each sample (see "Results"). Pyrosequencing thus provides higher sensitivity, robustness and throughput for

the analysis of *IDH1/2* mutation than Sanger sequencing [7]. Although the consistency between pyrosequencing and IHC needs further validation, pyrosequencing enables rapid screening for *IDH1/2* mutations (about 3–4 h) in a setting where DNA samples are already extracted. Ultimately, the optimal method for *IDH1/2* testing also depends on criteria such as the purpose of each study and/or the types of specimens available.

In summary, we have established a robust and sensitive assay for the detection of *IDH1/2* mutations. Our pyrosequencing assays are suitable for the analysis of a large number of samples, particularly if the samples are all simultaneously investigated such as in a large-scale retrospective clinical study.

Acknowledgments The authors thank Dr. Sylvia Kocialkowski for critical reading of the manuscript. This work was supported by JSPS KAKENHI Grant Numbers 24659650 (H. A.), 25462283 (K. I.) and by the National Cancer Center Research and Development Fund 23-A-50 (K. I.).

References

1. Agarwal S, Sharma MC, Jha P, Pathak P, Suri V, Sarkar C, Chosdol K, Suri A, Kale SS, Mahapatra AK (2013) Comparative study of IDH1 mutations in gliomas by immunohistochemistry and DNA sequencing. Neuro Oncol 15:718–726
2. Arita H, Narita Y, Fukushima S, Tateishi K, Matsushita Y, Yoshida A, Miyakita Y, Ohno M, Collins VP, Kawahara N, Shibui S, Ichimura K (2013) Upregulating mutations in the TERT promoter commonly occur in adult malignant gliomas and are strongly associated with total 1p19q loss. Acta Neuropathol 126:267–276
3. Balss J, Meyer J, Mueller W, Korshunov A, Hartmann C, von Deimling A (2008) Analysis of the IDH1 codon 132 mutation in brain tumors. Acta Neuropathol 116:597–602
4. Capper D, Zentgraf H, Balss J, Hartmann C, von Deimling A (2009) Monoclonal antibody specific for IDH1 R132H mutation. Acta Neuropathol 118:599–601
5. Choi J, Lee EY, Shin KJ, Minn YK, Kim J, Kim SH (2013) IDH1 mutation analysis in low cellularity specimen: a limitation of diagnostic accuracy and a proposal for the diagnostic procedure. Pathol Res Pract 209:284–290
6. Cykowski MD, Allen RA, Fung KM, Harmon MA, Dunn ST (2012) Pyrosequencing of IDH1 and IDH2 mutations in brain tumors and non-neoplastic conditions. Diagn Mol Pathol 21:214–220
7. Felsberg J, Wolter M, Seul H, Friedensdorf B, Goppert M, Sabel MC, Reifenberger G (2010) Rapid and sensitive assessment of the IDH1 and IDH2 mutation status in cerebral gliomas based on DNA pyrosequencing. Acta Neuropathol 119:501–507
8. Fukushima S, Narita Y, Miyakita Y, Ohno M, Takizawa T, Takusagawa Y, Mori M, Ichimura K, Tsuda H, Shibui S (2013) A case of more than 20 years survival with glioblastoma, and development of cavernous angioma as a delayed complication of radiotherapy. Neuropathology 33:576–581
9. Gravendeel LA, Kloosterhof NK, Bralten LB, van Marion R, Dubbink HJ, Dinjens W, Bleeker FE, Hoogenraad CC, Michiels E, Kros JM, van den Bent M, Smitt PA, French PJ (2010) Segregation of non-p.R132H mutations in IDH1 in distinct molecular subtypes of glioma. Hum Mutat 31:E1186–E1199
10. Hartmann C, Meyer J, Balss J, Capper D, Mueller W, Christians A, Felsberg J, Wolter M, Mawrin C, Wick W, Weller M, Herold-Mende C, Unterberg A, Jeuken JW, Wesseling P, Reifenberger G, von Deimling A (2009) Type and frequency of IDH1 and IDH2 mutations are related to astrocytic and oligodendroglial differentiation and age: a study of 1,010 diffuse gliomas. Acta Neuropathol 118:469–474
11. Horbinski C (2013) What do we know about IDH1/2 mutations so far, and how do we use it? Acta Neuropathol 125:621–636
12. Ichimura K, Pearson DM, Kocialkowski S, Backlund LM, Chan R, Jones DT, Collins VP (2009) IDH1 mutations are present in the majority of common adult gliomas but rare in primary glioblastomas. Neuro Oncol 11:341–347
13. Johnson BE, Mazor T, Hong C, Barnes M, Aihara K, McLean CY, Fouse SD, Yamamoto S, Ueda H, Tatsuno K, Asthana S, Jalbert LE, Nelson SJ, Bollen AW, Gustafson WC, Charron E, Weiss WA, Smirnov IV, Song JS, Olshen AB, Cha S, Zhao Y, Moore RA, Mungall AJ, Jones SJ, Hirst M, Marra MA, Saito N, Aburatani H, Mukasa A, Berger MS, Chang SM, Taylor BS, Costello JF (2014) Mutational analysis reveals the origin and therapy-driven evolution of recurrent glioma. Science 343:189–193
14. Kaneko MK, Morita S, Tsujimoto Y, Yanagiya R, Nasu K, Sasaki H, Hozumi Y, Goto K, Natsume A, Watanabe M, Kumabe T, Takano S, Kato Y (2013) Establishment of novel monoclonal antibodies KMab-1 and MMab-1 specific for IDH2 mutations. Biochem Biophys Res Commun 432:40–45
15. Kato Y, Jin G, Kuan CT, McLendon RE, Yan H, Bigner DD (2009) A monoclonal antibody IMab-1 specifically recognizes IDH1R132H, the most common glioma-derived mutation. Biochem Biophys Res Commun 390:547–551
16. Kato Y, Natsume A, Kaneko MK (2013) A novel monoclonal antibody GMab-m1 specifically recognizes IDH1-R132G mutation. Biochem Biophys Res Commun 432:564–567
17. Lee D, Suh YL, Kang SY, Park TI, Jeong JY, Kim SH (2013) IDH1 mutations in oligodendroglial tumors: comparative analysis of direct sequencing, pyrosequencing, immunohistochemistry, nested PCR and PNA-mediated clamping PCR. Brain Pathol 23(3):285–293
18. Louis DN, Ohgaki H, Wiestler OD, Cavenee WK, Burger PC, Jouvet A, Scheithauer BW, Kleihues P (2007) The 2007 WHO classification of tumours of the central nervous system. Acta Neuropathol 114:97–109
19. Malley DS, Hamoudi RA, Kocialkowski S, Pearson DM, Collins VP, Ichimura K (2011) A distinct region of the MGMT CpG island critical for transcriptional regulation is preferentially methylated in glioblastoma cells and xenografts. Acta Neuropathol 121:651–661
20. Mascelli S, Raso A, Biassoni R, Severino M, Sak K, Joost K, Milanaccio C, Barra S, Grillo-Ruggieri F, Vanni I, Consales A, Cama A, Capra V, Nozza P, Garre ML (2012) Analysis of NADP+ -dependent isocitrate dehydrogenase-1/2 gene mutations in pediatric brain tumors: report of a secondary anaplastic astrocytoma carrying the IDH1 mutation. J Neurooncol 109:477–484
21. Mikeska T, Bock C, El-Maarri O, Hubner A, Ehrentraut D, Schramm J, Felsberg J, Kahl P, Buttner R, Pietsch T, Waha A (2007) Optimization of quantitative MGMT promoter methylation analysis using pyrosequencing and combined bisulfite restriction analysis. J Mol Diagn 9:368–381
22. Morimura T, Neuchrist C, Kitz K, Budka H, Scheiner O, Kraft D, Lassmann H (1990) Monocyte subpopulations in human gliomas: expression of Fc and complement receptors and correlation with tumor proliferation. Acta Neuropathol 80:287–294

23. Ogino S, Kawasaki T, Brahmandam M, Yan L, Cantor M, Namgyal C, Mino-Kenudson M, Lauwers GY, Loda M, Fuchs CS (2005) Sensitive sequencing method for KRAS mutation detection by Pyrosequencing. J Mol Diagn 7:413–421
24. Ronaghi M, Uhlen M, Nyren P (1998) A sequencing method based on real-time pyrophosphate. Science 281(363):365
25. Sanson M, Marie Y, Paris S, Idbaih A, Laffaire J, Ducray F, El Hallani S, Boisselier B, Mokhtari K, Hoang-Xuan K, Delattre JY (2009) Isocitrate dehydrogenase 1 codon 132 mutation is an important prognostic biomarker in gliomas. J Clin Oncol 27:4150–4154
26. Setty P, Hammes J, Rothamel T, Vladimirova V, Kramm CM, Pietsch T, Waha A (2010) A pyrosequencing-based assay for the rapid detection of IDH1 mutations in clinical samples. J Mol Diagn 12:750–756
27. Thon N, Eigenbrod S, Kreth S, Lutz J, Tonn JC, Kretzschmar H, Peraud A, Kreth FW (2012) IDH1 mutations in grade II astrocytomas are associated with unfavorable progression-free survival and prolonged postrecurrence survival. Cancer 118:452–460
28. van den Bent MJ, Hartmann C, Preusser M, Strobel T, Dubbink HJ, Kros JM, von Deimling A, Boisselier B, Sanson M, Halling KC, Diefes KL, Aldape K, Giannini C (2013) Interlaboratory comparison of IDH mutation detection. J Neurooncol 112:173–178
29. von Deimling A, Korshunov A, Hartmann C (2011) The next generation of glioma biomarkers: MGMT methylation, BRAF fusions and IDH1 mutations. Brain Pathol 21:74–87
30. Watanabe T, Nobusawa S, Kleihues P, Ohgaki H (2009) IDH1 mutations are early events in the development of astrocytomas and oligodendrogliomas. Am J Pathol 174:1149–1153
31. Yan H, Parsons DW, Jin G, McLendon R, Rasheed BA, Yuan W, Kos I, Batinic-Haberle I, Jones S, Riggins GJ, Friedman H, Friedman A, Reardon D, Herndon J, Kinzler KW, Velculescu VE, Vogelstein B, Bigner DD (2009) IDH1 and IDH2 mutations in gliomas. N Engl J Med 360:765–773
32. Yan W, Zhang W, You G, Bao Z, Wang Y, Liu Y, Kang C, You Y, Wang L, Jiang T (2012) Correlation of IDH1 mutation with clinicopathologic factors and prognosis in primary glioblastoma: a report of 118 patients from China. PLoS ONE 7:e30339

Journal of Radiation Research, 2014, 55, 803–811
doi: 10.1093/jrr/rru017 Advance Access Publication 27 March 2014

Inflammation as well as angiogenesis may participate in the pathophysiology of brain radiation necrosis

Erina YORITSUNE[1], Motomasa FURUSE[1], Hiroko KUWABARA[2], Tomo MIYATA[1], Naosuke NONOGUCHI[1], Shinji KAWABATA[1], Hana HAYASAKI[3], Toshihiko KUROIWA[1], Koji ONO[4], Yuro SHIBAYAMA[2] and Shin-Ichi MIYATAKE[1,*]

[1]Department of Neurosurgery, Division of Life Sciences, Osaka Medical College, 2-7 Daigaku-machi, Takatsuki City, Osaka 569-8686, Japan
[2]Department of Pathology, Division of Life Sciences, Osaka Medical College, 2-7 Daigaku-machi, Takatsuki City, Osaka 569-8686, Japan
[3]Department of Anatomy and Cell Biology, Division of Life Sciences, Osaka Medical College, 2-7 Daigaku-machi, Takatsuki City, Osaka 569-8686, Japan
[4]Particle Radiation Oncology Research Center, Research Reactor Institute, Kyoto University, Japan
*Corresponding author. Department of Neurosurgery, Osaka Medical College, 2-7 Daigaku-machi, Takatsuki City, Osaka 569-8686, Japan. Tel: +81-72-683-1221; Fax: +81-72-681-3723; Email: neu070@poh.osaka-med.ac.jp

(Received 13 September 2013; revised 14 February 2014; accepted 21 February 2014)

Radiation necrosis (RN) after intensive radiation therapy is a serious problem. Using human RN specimens, we recently proved that leaky angiogenesis is a major cause of brain edema in RN. In the present study, we investigated the same specimens to speculate on inflammation's effect on the pathophysiology of RN. Surgical specimens of symptomatic RN in the brain were retrospectively reviewed by histological and immunohistochemical analyses using hematoxylin and eosin (H&E) staining as well as immunohistochemical staining for VEGF, HIF-1α, CXCL12, CXCR4, GFAP, CD68, hGLUT5, CD45, IL-1α, IL-6 TNF-α and NF-*k*B. H&E staining demonstrated marked angiogenesis and cell infiltration in the perinecrotic area. The most prominent vasculature was identified as thin-walled leaky angiogenesis, i.e. telangiectasis surrounded by prominent interstitial edema. Two major cell phenotypes infiltrated the perinecrotic area: GFAP-positive reactive astrocytes and CD68/hGLUT5-positive cells (mainly microglias). Immunohistochemistry revealed that CD68/hGLUT5-positive cells and GFAP-positive cells expressed HIF-1α and VEGF, respectively. GFAP-positive cells expressed chemokine CXCL12, and CD68/hGLUT5-positive cells expressed receptor CXCR4. The CD68/hGLUT5-positive cells expressed pro-inflammatory cytokines IL-1α, IL-6 and TNF-α in the perinecrotic area. VEGF caused leaky angiogenesis followed by perilesional edema in RN. GFAP-positive cells expressing CXCL12 might attract CXCR4-expressing CD68/hGLUT5-positive cells into the perinecrotic area. These accumulated CD68/hGLUT5-positive cells expressing pro-inflammatory cytokines seemed to aggravate the RN edema. Both angiogenesis and inflammation might be caused by the regulation of HIF-1α, which is well known as a transactivator of VEGF and of the CXCL12/CXCR4 chemokine axis.

Keywords: brain radiation necrosis; CXCL12/CXCR4 chemokine axis; inflammation; microglia; pro-inflammatory cytokine

INTRODUCTION

Radiotherapeutic technologies have progressed in recent decades; patients with malignant brain tumors can now be treated with high-dose irradiation with good conformity, prolonging their survival. On the other hand, brain radiation necrosis (RN), a late adverse effect of radiation therapies, has become a serious problem, and existing treatments for brain RN have not been sufficiently effective. Recently, bevacizumab (BV), an antibody to vascular endothelial growth factor (VEGF), has received attention as a promising treatment for RN [1–3]. BV shows sharp and potent treatment effects. On

the basis of our analysis of human RN surgical specimens, we previously demonstrated that edema in RN is caused by VEGF overexpression in reactive astrocytes [4]. However, the effects are often temporary; RN occasionally recurs after BV treatments [1]. Therefore, to overcome this intractable pathology, it will be necessary to elucidate its underlying mechanisms.

In a recent study using human RN specimens, we proved that 'leaky' angiogenesis is a major cause of brain edema in RN [4], as shown in Fig. 1 in this report. Furthermore, we have discovered that GFAP-positive and CD68-positive cells accumulate around the circumference of the RN core, i.e. the perinecrotic area [5]. In addition, we have shown that HIF-1α and VEGF participate in the formation of angiogenesis, microbleeding, and interstitial edema at the RN circumference [4]. However, it remains to be determined why these GFAP-positive cells and CD68-positive cells accumulate in the perinecrotic area, which cells express VEGF and HIF-1α in RN, and whether or not other molecules participate in the pathophysiology of RN.

In malignant tumors (including glioblastomas) the CXCL12/CXCR4 chemokine axis is known to be correlated with HIF-1α and VEGF expression [6, 7]. Furthermore, the involvement of chronic inflammation has also been suggested as a mechanism (in addition to angiogenesis) underlying brain RN [8]. The aim of the present study is to elucidate the molecular mechanisms underlying brain RN in humans, with special reference to angiogenesis and inflammation. We also speculated on the potential relationship between chemokine and cytokine expression and accumulation in GFAP, CD68, hGLUT5 and CD45-positive cells in the perinecrotic area. Here, GFAP, CD68, hGLUT5 and CD45 were adopted as markers for astrocytes, monocytes, microglias and lymphocytes, respectively. The study design consisted of a retrospective qualitative review with histological and immunohistochemical analyses of surgical specimens from the brains of patients with symptomatic RN treated in our department.

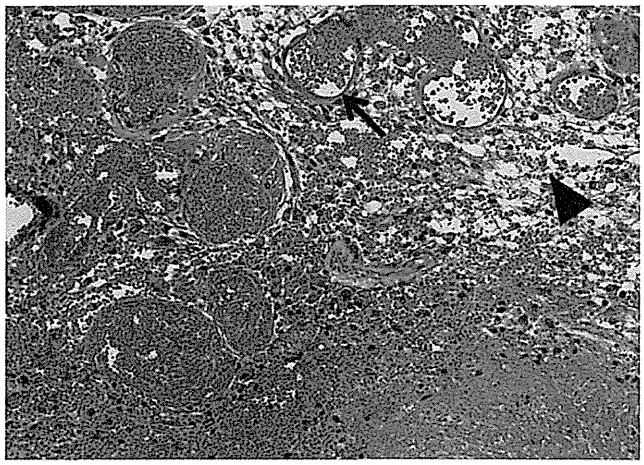

Figure 1. A hematoxylin and eosin (H&E)-stained specimen from Case 5. Thin-walled enlarged capillaries indicating telangiectasis (arrow) and the proliferation of arterioles can be seen in the area between the necrotic core and normal brain tissue. These blood vessels were accompanied by interstitial edema (arrowhead) due to plasma leakage. The original objective magnification was ×100.

MATERIALS AND METHODS

Specimens

Surgical specimens of seven patients with symptomatic RN in the brain who had been treated in our department from 2006 through 2009 were subjected to histological and immunohistochemical analyses. The study was approved by the Osaka Medical College Ethics Committee, and we obtained informed consent from all of the patients prior to surgeries and procedures. All of the patients had received radiation therapy, including X-ray treatment, stereotactic radiosurgery (SRS), and/or boron neutron capture therapy [9–13]. They also had received some medical treatments for RN, including corticosteroids, anticoagulants, and so on, for at least one month; however, the symptoms were refractory to these medical treatments. The original diseases were two head and neck cancers, four glioblastomas, and one metastatic brain tumor derived from breast cancer. Both patients with head and neck cancers had only extracranial tumors without infiltration and/or metastasis to the brain. Their irradiation fields included not only the original head and neck cancers but also some part of the temporal lobe. Therefore, these were samples of pure RN without the presence of tumor cells in the temporal lobe. Brain RN in all cases was diagnosed by pathological examination of the surgical specimen (Table 1).

Tissue preparation and immunohistochemistry

Tissue samples were fixed in 10% buffered formalin and embedded in paraffin. Tissue sections were cut (4-μm slices), deparaffinized with xylene, and rehydrated through graduated ethanol solutions. One section of each sample was stained with hematoxylin and eosin (H&E), and the other sections were used for HIF-1α, VEGF, CXCL12, CXCR4, IL-1α, IL-6, TNF-α, GFAP, CD68, hGLUT5, CD45 and NF-κB staining by the biotin–streptavidin–peroxidase method. Here, GFAP, CD68, hGLUT5 and CD45 were adopted as markers for astrocytes, monocytes, microglias and lymphocytes, respectively, as described above. Deparaffinized and rehydrated sections were subjected to pressure boiling for antigen retrieval in antigen unmasking solution. These sections were incubated with 0.03% hydrogen peroxidase for 5 min at room temperature to block endogenous peroxidase activity. The sections were then incubated with one of the above 12 primary antibodies at 4°C overnight. The information on these primary antibodies, including dilutions, is summarized in Table s1. The sections were then incubated with peroxidase-labeled secondary antibody (Dako) for 30 min at room temperature.

Table 1. Patient profile of symptomatic radiation necrosis

Case	Age	Gender	Original dis.[a]	Radiation[b]	Duration[c]	Chemotherapy[d]
1	78	M	Sal. Duc. Ca.	XRT (60 Gy), BNCT × 2 (6.1 and 10.1 Gy-Eq)	20	
2	46	F	Ade. Ca.	XRT (60 Gy), BNCT × 2 (6.9 and 6.7 Gy-Eq)	7	MTX, UFT, CDDP
3	69	F	GB	XRT (60 Gy), BNCT (13.3 Gy-Eq)	3	ACNU
4	68	F	GB	XRT (60 Gy), BNCT (9.67 Gy-Eq)	12	
5	46	M	GB	XRT (60 Gy), BNCT (13.7 Gy-Eq)	5	PCV
6	39	M	GB	XRT (60 Gy), SRS (18 Gy)	8	ACNU
7	54	F	Ade. Ca.	SRS (22 Gy)	9	Herceptin

[a]Sal. Duc. Ca. = salivary ductal carcinoma, GB = glioblastoma, Ade. Ca. = adenocarcinoma. [b]XRT = X-ray treatment, BNCT = boron neutron capture therapy, SRS = stereotactic radiosurgery, Gy-Eq = biologically equivalent X-ray dose that would have equivalent effects on tumor and normal brain. In BNCT, the presented dose is the peak point dose for normal brain. In SRS, the presented dose is the marginal X-ray or gamma-ray dose. BNCT × 2 means intentional fractionated BNCT in two sessions. [c]Months between termination of last radiotherapy and onset of symptoms caused by radiation necrosis. Radiation necrosis in Cases 1 and 2 occurred in temporal lobes and was included in the irradiation fields. [d]MTX = methotrexate, UFT = combined drug of tegafur and uracil, CDDP = cisplatin, ACNU = nimustin, PCV = procarbazine, nimustin, vincristine.

They were developed with diaminobenzidine, lightly counterstained with hematoxylin, and mounted.

Double immunofluorescence microscopy

Double immunofluorescence staining was performed using the following antibody combinations: CXCL12 and GFAP or CD68, CXCR4 and GFAP or CD68, HIF-1α and GFAP or CD68, VEGF and GFAP or CD68, IL-1α and GFAP or CD68, IL-6 and GFAP or CD68, TNF-α and GFAP or CD68, hGLUT5 and CD68 or CXCR4 or IL-1α or HIF-1α, and CD45 and IL-1α or CXCR4. The secondary antibodies used were Alexa Fluor 488 goat anti-mouse IgG, Alexa Fluor 488 goat anti-rabbit IgG, Alexa Fluor 546 goat anti-mouse IgG, and Alexa Fluor 546 goat anti-rabbit IgG (Invitrogen, Carlsbad, CA). These were examined using an LSM510 laser scanning confocal microscope (Carl Zeiss, Oberkochen, Germany).

RESULTS

Histochemical analysis with H&E staining

Figure 1 shows a typical finding of H&E staining of RN from Case 5. Remarkable angiogenesis existed in the perinecrotic area. The most prominent vasculature was identified as a thin-walled, leaky angiogenesis, such as telangiectasis with prominent interstitial edema, which is consistent with our previous study [4]. The interstitial edema was probably caused by leakage of the plasma from the fragile angiogenesis. There was no cytoarchitecture in the core of the necrotic foci, whereas some infiltrating cells were observed in the perinecrotic area, as indicated with hematoxylin-stained nuclei. Of course, the incidence of RN is generally affected by the applied radiation dose, distribution, and adjuvant chemotherapy [14, 15]. However, these are universal pathological findings, irrespective of the original tumor types and radiation modalities, as we reported previously [4].

Immunohistochemical analysis of the localization of CXCL12, CXCR4, GFAP, CD68, IL-1α, IL-6, TNF-α, NF-κB, hGLUT5 and CD45

We next sought to determine the cell types (i.e. astrocytes or monocytes) that produce chemokines and/or express the corresponding receptors. To this end, we performed enzyme-immunohistochemical analyses for gross identification of the infiltrative cells and proteins expressed using the primary antibodies described in Materials and Methods. H&E staining was also performed on each specimen to identify the necrotic core, the perinecrotic area, and the normal brain area. The specimens obtained from Cases 2 and 3 demonstrate representative findings for the expression of GFAP, CD68, CXCL12 and CXCR4 (Fig. 2). As we reported previously [5], two major cell phenotypes infiltrated the perinecrotic area: GFAP-positive astrocytes and CD68-positive monocytes. We observed similar distributions of GFAP-positive cells and CXCL12-positive cells; CD68-positive cells and CXCR4-positive cells were also similarly distributed. The former cell type was limited mainly to the perinecrotic area, whereas the latter population was observed not only in the perinecrotic area but also, though to a lesser degree, in the necrotic core. The same tendencies were observed among all cases (data not shown).

To evaluate the distribution of cytokine production in RN, we performed immunohistochemical staining for IL-1α, IL-6 and TNF-α. The specimens obtained from all cases revealed oval cells positive for IL-1α, IL-6 and TNF-α in the perinecrotic area (data not shown). These cells also appeared inside the necrotic